

# MODELING OF MOLECULAR ADSORPTION AND ORGANIZATION AT LIQUID-SOLID INTERFACES AND INTERACTIONS OF MOLECULES IN LIQUIDS

R.HENTSCHKE

*Max-Planck-Institut für Polymerforschung*

*Ackermannweg 10*

*55128 Mainz*

*Germany*

**ABSTRACT.** Interfaces between liquids and solid surfaces are of considerable scientific as well as technological interest, in particular, in the context of the adsorption and organization of molecular films. In recent years the direct observation of the molecular structure and often even the dynamics of ordered monolayers at such hidden interfaces has been made possible by the rapid development in scanning probe microscopy. Nevertheless, there is still a lack of understanding with respect to the formation and organization of such films and their interaction with the experimental apparatus. Here computer modeling plays an increasing role as both the complexity of the interfaces and the available computer power increase. In this article I use three examples to discuss some aspects of the application of computer as well as analytical modeling in the context of monolayer formation, its structural behavior at the liquid-solid interface and, in addition, the computer modeling of interactions across a macromolecule-solvent-macromolecule interface.

## 1. Introduction

In recent years there has been a rapid development in the application of scanning probe microscopies to the study of highly ordered molecular films adsorbed on solid substrates (see e.g., <sup>1</sup>). Such films, often prepared via simple self-assembly when the molecules adsorb on the substrate from solution, are of interest in areas ranging from lubrication and colloidal stability over molecular recognition to tailoring the surface and interfacial properties of semiconductors <sup>2</sup>. Theoretical work on this subject currently lags behind in two key aspects, i.e. the *ab initio* prediction of the surface structure formed by a given type of molecule at a given interface as well as the relation between the observed tunneling or surface force contrasts and the atomic detail of the interfacial layer. The examples discussed in this article mainly focus on the former aspect. More precisely, I will be concerned with the type of system depicted in figure 1, which shows a sketch of a highly ordered physisorbed layer consisting of short chain molecules at the interface between a smooth solid surface and a solution from which the solute molecules were adsorbed onto the surface.

Analytical theoretical models of adsorption from solution are usually based on either lattice descriptions of both surface and solution or on assuming homogeneous structureless surfaces in equilibrium with likewise structureless liquids (e.g., <sup>3</sup>). The added complexity if one wants to include molecular detail, however, makes the use of computer simulation techniques like Monte Carlo (MC) or Molecular Dynamics (MD) virtually indispensable. There are numerous simulation studies of the solid-(monolayer) adsorbate-vacuum interface mostly for rare gases and small molecules, focusing on the translational and orientational ordering and dynamics as well as on universal and non-universal aspects of surface phase transitions, applying both MC as well as MD. Some examples, where graphite, on which we will mainly focus here, is used as substrate, are Kr <sup>4</sup> or Ar <sup>5</sup>, small linear molecules like N<sub>2</sub> <sup>6</sup> or CS<sub>2</sub> <sup>7</sup>, polar molecules like CH<sub>3</sub>F or CH<sub>3</sub>Cl <sup>8</sup>, and various hydrocarbons like methane<sup>9</sup>, ethylene <sup>10</sup>, ethane <sup>11</sup>, benzene <sup>12</sup>, butane <sup>13</sup>, hexane <sup>14</sup> or decane <sup>13</sup>. For dense physisorbed layers composed of larger molecules, however, the straightforward simulation, starting from an arbitrary molecular arrangement, which during the simulation develops into the thermodynamically

stable structure, including surface induced segregation, adsorption, and, possibly translational and/or orientational ordering within the interface, is much more difficult. It is worth emphasizing that the inclusion of the third dimension, i.e. the entire solid-solution interface, is necessary as a pathway for achieving the dense molecular arrangement on the surface<sup>15,16</sup>, even though the coupling of the equilibrium monolayer structure to the adjacent solution may be weak<sup>17,16</sup>.

Here I discuss the modeling of such interface phenomena in terms of three examples. The first two are focused on the structural behavior of short chain molecules near smooth surfaces, i.e. the simulation of the physisorption of short n-alkanes from benzene onto graphite and the analytical modeling of the structural phase behavior within the subsequently formed dense monolayers and its observation using STM. The third example, which is somewhat removed from the other two, addresses the molecular modeling of the effective interaction forces between segments of a rigid rod macromolecule in solution, which, in the present case, is a helical polypeptide frequently used in the preparation of molecular films on solid substrates.

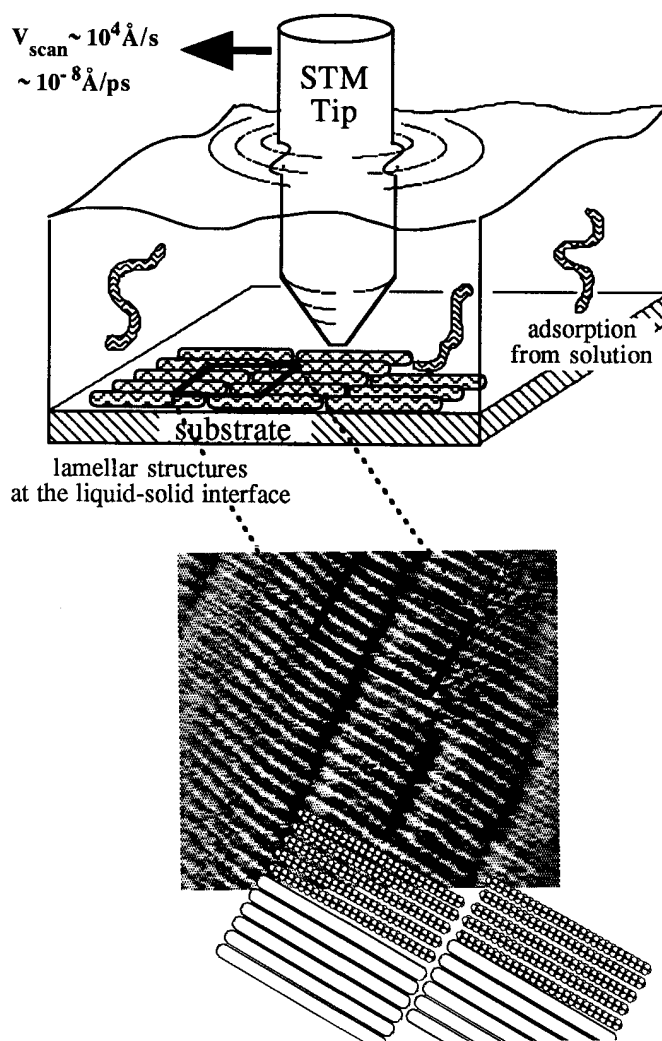


**Figure 1:** Top: Sketch of an STM tip scanning across a highly ordered alkane monolayer adsorbed at a liquid-solid interface.  $v_{\text{scan}}$  is the tip's velocity in a fast scanning mode<sup>18</sup>. Bottom: A corresponding real STM image (taken from<sup>19</sup>) showing a crystalline monolayer, which consists of long and short alkanes (i. e.  $\text{C}_{50}\text{H}_{102}$  and  $\text{C}_{25}\text{H}_{52}$ ) at the interface between 1-phenyloctane and graphite (cf. below). The sketch at the bottom illustrates molecular models of different refinement.

## 2. Short chain molecules at the liquid-solid interface: adsorption and phase behavior of alkanes on graphite

### 2.1 Adsorption of short chain alkanes from benzene onto graphite - the molecular dynamics approach

In the simplest case, MD stands for the numerical integration of the classical equations of motion governing the system of interest<sup>20-22</sup>. The force on the individual atoms (all atom method) or clusters of atoms 'condensed' into single pseudo-atoms (united atom method) is calculated based on phenomenological force fields, which should be simple enough to allow their frequent numerical evaluation, but still sufficiently accurate to reproduce the phenomena of interest. For liquid-solid interfaces it is convenient to separate the interactions in three contributions, i.e. the intra-adsorbate or intra-liquid interaction, the adsorbate-solid or liquid-solid interaction, and the intra-solid interaction. Whether the latter is a necessary ingredient depends on the type of system and on the problem. For instance, the interaction of the liquid with the solid might cause the surface to relax or reconstruct, or the dynamics of the solid might couple to the adsorbate, or, more importantly, two solid surfaces might deform elastically or inelastically on contact, like when a STM or SFM tip is in immediate contact with the surface. These cases can often be treated successfully by modeling the solid's cohesive energy in terms of the embedded atom method (cf. the article by L. Dagens in reference<sup>21</sup>; see also reference<sup>23</sup>, where this method is applied). However, here we will be dealing with problems where the intra-solid contribution can be safely neglected, and the potential, which is used in the following, is given by

$$\begin{aligned}
 V = & \sum_{bonds} f_r (r - r_{eq})^2 + \sum_{angles} f_\delta (\delta - \delta_{eq})^2 + \sum_{dihedral} f_n \{1 + \cos(n\phi - \gamma)\} \\
 & + \sum_{i < j} \sqrt{\epsilon_i \epsilon_j} \left\{ \left( \frac{\sigma_i + \sigma_j}{r_{ij}} \right)^{12} - 2 \left( \frac{\sigma_i + \sigma_j}{r_{ij}} \right)^6 \right\} + \sum_{i < j} \frac{q_i q_j}{r_{ij}} \\
 & + \sum_i V_{surf}(\vec{r}_i)
 \end{aligned} \tag{1}$$

The first three terms are bonding intra-adsorbate interactions encompassing harmonic bond stretch and valence angle potentials as well as a cosine-type torsional potential. The next two non-bonded interaction terms describe electronic overlap and dispersion interactions via a simple 12-6 Lennard-Jones (LJ) potential and Coulomb interactions between atomic partial charges within the adsorbate. Notice that using the Lorentz-Berthelot mixing rules<sup>20</sup> the usual LJ parameters  $\epsilon_{ij}$  and  $\sigma_{ij}$  are expressed as  $\epsilon_{ij} = \sqrt{\epsilon_i \epsilon_j}$  and  $\sigma_{ij} = \sigma_i + \sigma_j$ , where the indices label the interacting atoms and a factor 1/2 on the right hand side of the expression for  $\sigma_{ij}$  has been absorbed into  $\sigma_i$  and  $\sigma_j$ . These terms constitute the so called AMBER (Assisted Model Building with Energy Refinement) potential, one of several widely used "general purpose" potential functions for molecular systems<sup>24,25</sup>. Notice that following reference<sup>24</sup> the above 1-4 LJ and 1-4 Coulomb interactions, i.e. interactions between sites separated by three bonds, are scaled by a factor 1/2. Also, when there are hydrogen bonds to consider, there will be an additional 10-12 potential term (cf. below). For many standard cases, the parameters (like force constants, equilibrium bond lengths and bond angles) appearing in these terms are tabulated in the above references, with the exception of the partial charges, which must be calculated separately.

The last term in equation (1) describes the surface potential acting on an adsorbate atom of type  $\alpha$  located at the position  $\vec{r}_{i_\alpha} = (x_{i_\alpha}, y_{i_\alpha}, z_{i_\alpha})$  with respect to some origin on the surface. Here  $z_{i_\alpha}$  is the

perpendicular distance measured from the topmost layer of atoms in the solid. In the simplest case, the interaction between an adsorbate atom of type  $\alpha$  and a substrate atom of type  $\beta$  separated by a distance  $r_{\alpha\beta}$  can be approximated in terms of LJ pair interactions, i.e. by  $\varepsilon_{\alpha\beta}\{(\sigma_{\alpha\beta}/r_{\alpha\beta})^{12} - 2(\sigma_{\alpha\beta}/r_{\alpha\beta})^6\}$ , where  $\varepsilon_{\alpha\beta}$  is the depth of the potential well and  $\sigma_{\alpha\beta}$  is the location of its minimum (cf. figure 3). As a first approximation of  $V_{surf}$  we may integrate these LJ interactions over the continuous half space replacing the solid instead of summing over discrete lattice sites. This yields

$$V_{surf}^{(9-3)}(z_{i\alpha}) = \sum_{\beta} \frac{\pi}{3} n_{\beta} \varepsilon_{\alpha\beta} \sigma_{\alpha\beta}^3 \left\{ \frac{1}{15} \left( \frac{\sigma_{\alpha\beta}}{z_{i\alpha}} \right)^9 - \left( \frac{\sigma_{\alpha\beta}}{z_{i\alpha}} \right)^3 \right\} \quad (2)$$

where  $n_{\beta}$  denotes the number density of  $\beta$ -atoms in the solid. The next better approximation is to smear out the solid's atoms only within the individual lattice planes parallel to the surface, which then yields

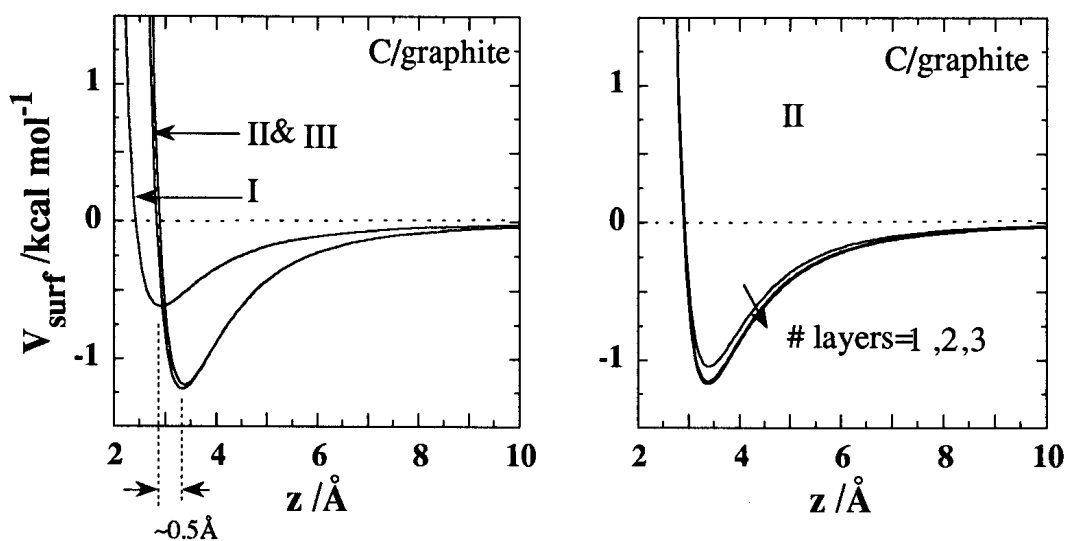
$$V_{surf}^{(0)}(z_i) = \sum_{\beta} \sum_{l=0}^{\infty} \pi n'_{\beta} \varepsilon_{\alpha\beta} \sigma_{\alpha\beta}^2 \left\{ \frac{1}{5} \left( \frac{\sigma_{\alpha\beta}}{z_i + d_l} \right)^{10} - \left( \frac{\sigma_{\alpha\beta}}{z_i + d_l} \right)^4 \right\} \quad (3)$$

where  $n'_{\beta}$  denotes the number density of  $\beta$ -atoms in the  $l$ th layer, and  $d_l$  is the  $z$ -position of the  $l$ th layer. Finally, one can employ the solid's translational symmetry and explicitly sum over all lattice sites. Such a calculation was carried out by Steele<sup>26</sup> for several surface geometries. The result can be written as

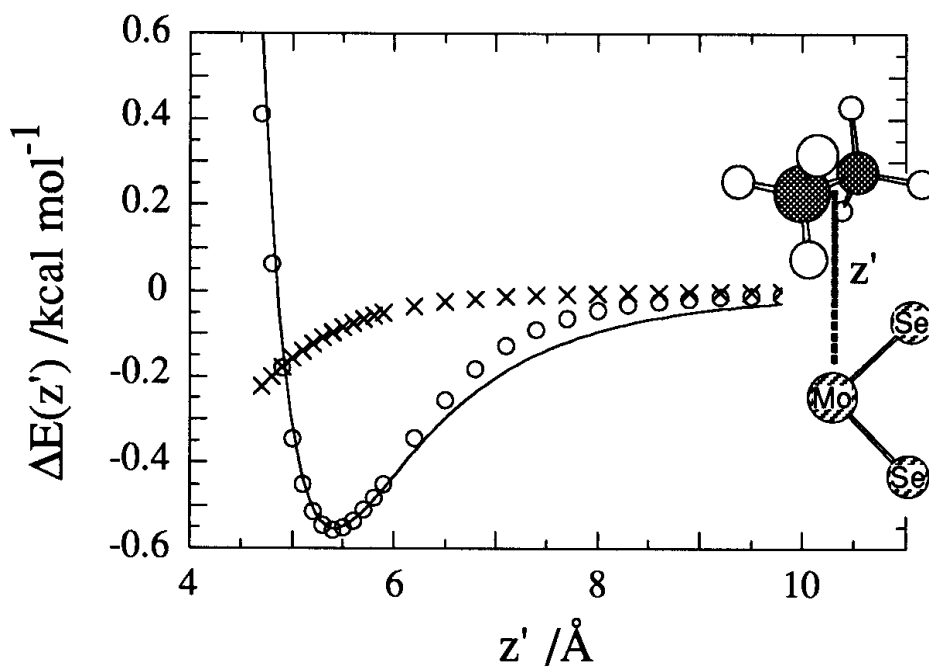
$$V_{surf}(\vec{r}_i) = V_{surf}^{(0)}(z_i) + \sum_{m=1}^{\infty} V_{surf}^{(m)}(\vec{r}_i) \quad (4)$$

where the right hand side of equation (4) is a sum over contributions from successively larger reciprocal neighbor shells corresponding to the two-dimensional surface lattice of interest. Notice that the first term is identically given by equation (3). The remaining terms,  $m=1, \dots, \infty$ , account for the corrugation of the surface. Explicit expressions for the  $V_{surf}^{(m)}$  can be found in the literature for the (100) and (111) fcc faces<sup>26</sup>, the graphite basal plane<sup>26</sup> and for a family of transition metal dichalcogenides<sup>27</sup>. Here we compare the three different potential expressions graphically for a single carbon atom interacting with the basal surface of graphite in figure 2. Notice that the effect of the corrugation is quite small compared to the overall depth of the surface potential well. Notice also that the continuum approximation (2) is not so good. In fact, due to the rapid convergence if successively deeper lying graphite planes are included (as illustrated in the right panel of figure 2) it is still better to approximate the surface potential by the contribution from one single surface plane only, i.e. by the  $l=0$  term in (3) (at virtually the same computational expense!).

Notice that the hydrocarbon-graphite LJ parameters used here are those of Battezzati et al.<sup>28</sup>, who obtain good agreement for the isosteric heat of adsorption for a number of small hydrocarbons using the potential (4). For an all-trans *n*-alkane (with its carbon zig-zag plane perpendicular to the graphite surface) the adsorption energy calculated with the same parameters is  $\sim 1.7$  kcal/mol for the  $\text{CH}_2$  groups ( $\sim 2.8 k_B T$  per  $\text{CH}_2$  group). The corresponding corrugation energy for, for instance,  $\text{C}_{24}\text{H}_{50}$  is  $< 4\%$  of the molecular adsorption energy<sup>17</sup>. In general, the calculation of the adsorbate-surface interaction parameters is not easy, especially in the case of more 'exotic' substrates than graphite. Figure 3, however, shows an example of an *ab initio* calculation of the interaction of ethane with a small substrate cluster,  $\text{MoSe}_2$ , where the quantum mechanical result can also be fitted quite well by LJ pair potentials.

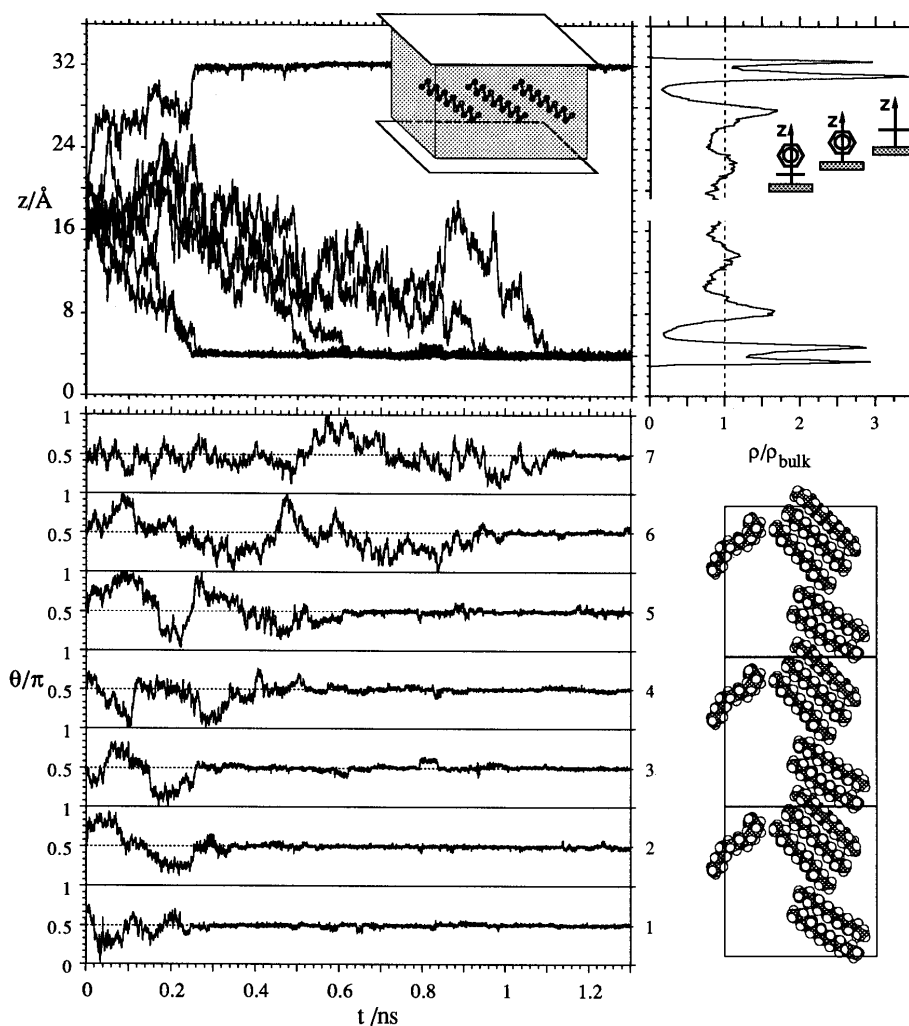


**Figure 2:** Distance dependence of the surface potential energy of a carbon atom above the basal plane of graphite. The carbon atom is located above the center of a hexagon. Here  $\epsilon=0.063\text{kcal/mol}$ ,  $\sigma=3.82\text{\AA}$ ,  $d_f=3.39\text{\AA}$ , and  $n_{\text{graphite}}=0.1126\text{\AA}^{-3}$  (cf. <sup>17</sup>). Left panel: Comparison of the two approximations (2) and (3) with the exact summation (4) indicated by I, II, and III, respectively. Right panel: Equation (3) plotted including only the terms with  $l \leq 0, 1$ , and 2, respectively, which corresponds to including only the first, the first two, and the first three layers of atoms.



**Figure 3:** Subtracted cluster energy  $\Delta E(z')=E_{\text{total}}(z')-E_{\text{total}}(\infty)$  vs.  $z'$  (cf. the dotted line in the insert). Circles: *ab initio* result; crosses: Coulomb contribution; solid line: fit to the difference between the quantum result and the Coulomb contribution based on LJ pair potentials between the atoms. The figure shows a result obtained by J. Burda in reference <sup>27</sup>.

The routine application of the MD method to the simulation of phenomena on the atomic level using a fast workstation (e.g., the calculations reported here were mainly done on DEC  $\alpha$ -VAX 400 and 600 workstations) without, for instance, parallelization etc., is still limited to a spatial scale  $L \leq 100 \text{ \AA}$  and a time scale  $\leq \text{ns}$  (e.g., the STM tip in figure 1 is virtually stationary during this time!). Notice in this context that the number of interactions, which have to be calculated at every simulation step, which itself must be significantly shorter than the inverse of the highest frequency in the system (usually between 0.5 and 5fs), is given roughly by  $M \approx 1/2 N^2 (2R_{cut}/L)^3$ , where  $N$  is the number of atoms or pseudo atoms contained in a  $L \times L \times L$  box and  $R_{cut}$  is a cutoff distance for the interactions. Typical numbers for the liquids in the present context are  $N \sim 2500$ -5000,  $R_{AA}$  (in general this depends on the range and the strength of the interactions), and  $L \sim 32$ -40  $\text{\AA}$ , and thus  $M \sim 4$ -8  $10^5$ ! These numbers are for 'all atom' simulations. If the 'united atom' approximation is applied,  $L$  can be increased by a factor  $\sim 1.5$ -2 for a liquid of alkanes for the same  $M$ . Thus, with respect to adsorption, this limits the method to still rather small adsorbates and fairly concentrated solutions.



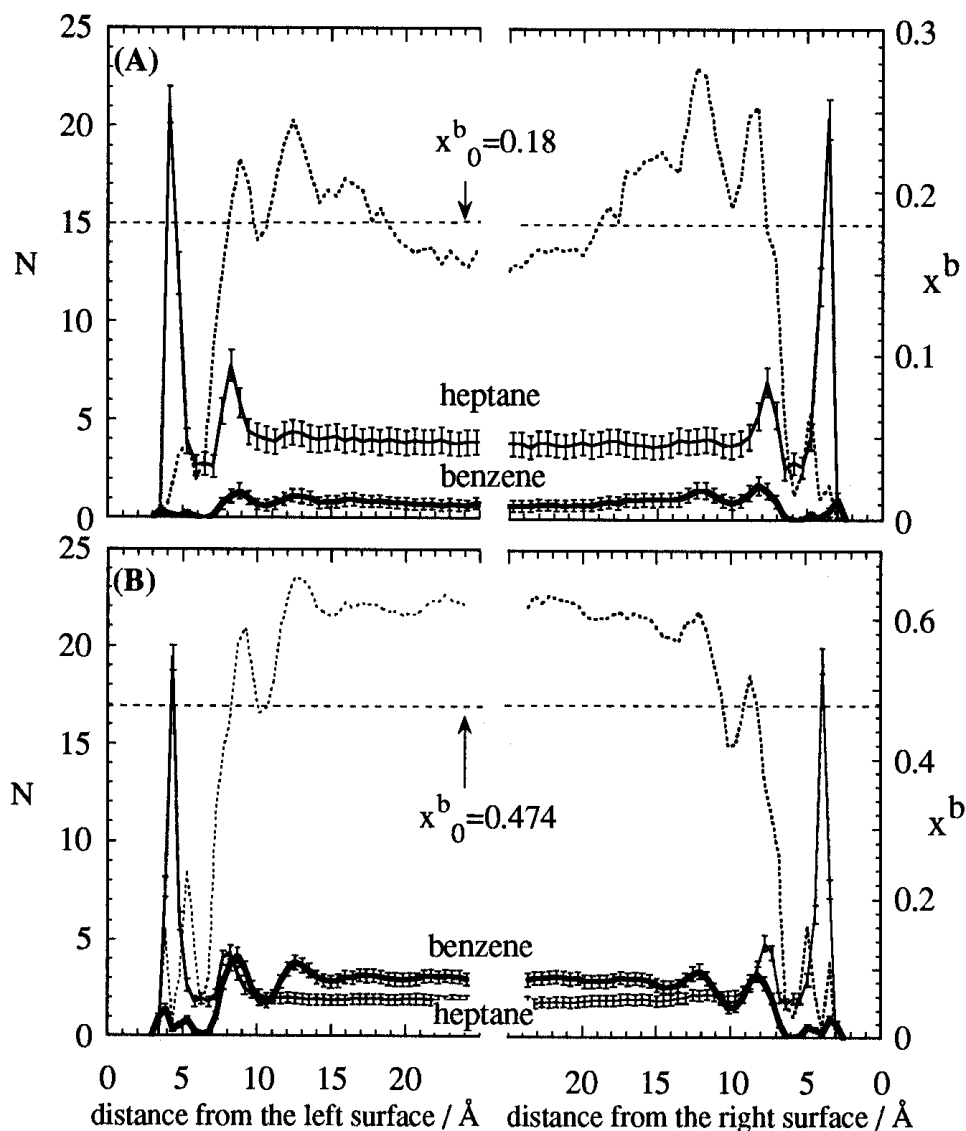
**Figure 4:** Adsorption of  $C_{14}H_{30}$  from benzene onto graphite. Upper left: Position  $z$  of the center of mass of each of the seven  $C_{14}H_{30}$  molecules perpendicular to the surfaces (at  $z=0 \text{ \AA}$  and  $z=36 \text{ \AA}$ ) as a function of time  $t$ . The insert shows a schematic of the system with only three solute molecules at  $t=0$ . Lower left:  $\Theta$ -trajectories of the individual  $C_{14}H_{30}$  molecules, where  $\Theta$  is the angle between a molecule's end-to-end vector and the surface normal, divided by  $\pi$ . Upper right: Unperturbed benzene center of mass density profile normal to the surface. The inserts illustrate the preferential molecular orientation and packing for the first three peaks. Lower right: The cluster of  $C_{14}H_{30}$  molecules adsorbed on the lower surface after 1.3ns including its neighboring periodic images. The solvent molecules are not shown.

Figure 4 summarizes a simulation, where a small number of  $C_{14}H_{30}$  molecules is adsorbed from benzene onto graphite<sup>29</sup>. The system consists of pre-equilibrated benzene at  $T=300K$  confined to a narrow slit formed by two parallel graphite surfaces with periodic boundaries applied parallel to the surfaces. Notice the pronounced surface induced solvation shell structure shown in the upper right panel in figure 4 taken from reference<sup>30</sup>, which describes a constant pressure simulation of the pure benzene-graphite system. Each peak can be attributed to a certain preferential orientation of the corresponding benzene molecules, as shown by the inserts, where the peak nearest to the surface corresponds to the topmost sketch and so on. At some point the simulation is stopped and seven  $C_{14}H_{30}$  molecules are inserted among 185 benzene molecules as shown schematically in the upper left panel. The same panel shows the temporal history of the centers of mass of the inserted molecules. Within  $\sim 1ns$  all  $C_{14}H_{30}$  molecules adsorb on the surfaces. The lower left panel shows that the chains adsorb with their molecular axes, defined by their end-to-end vector, parallel to the surface, where the chains assume stretched conformations with mean square end-to-end separations of about 90% of the all trans extension as compared to about 60% in the center of the slit<sup>29</sup>. Finally, the lower right of figure 4 shows the small cluster of adsorbed chains on the lower surface at the end of the simulation run. Notice that the cluster of extended chains lying side-by-side is formed even though there is sufficient area for the molecules to disperse on the surface. Notice also that the surface energy of densely adsorbed n-alkanes is actually only slightly higher than the corresponding energy for benzene. However, the interaction between neighboring alkanes constitutes a significant energetic advantage<sup>29</sup>. Obviously, the simulation potential captures two essential features, the adsorption from solution and the tendency for side-by-side association, which is a prerequisite for the lamella observed via STM (cf. figure 1). A larger but otherwise analogous simulation of a n-hexane/n-hexadecane mixture on Au(001) shows the tendency for the lamellar arrangement even more conclusively<sup>15</sup>.

The modeling of liquid mixtures near solid interfaces is of special interest. The different enthalpic and entropic interactions with the solid may cause segregation of the species and lead to a complex interfacial structure with not only different internal structure but also varying composition of the different surface induced solvation shells. Experimental investigations of such interfaces are difficult. Whereas tip microscopes possess high lateral resolution, their sensitivity to the tip-to-surface separation is not readily translated into useful information about the interface along the direction of the surface normal. Also, tip microscopy requires that the mobility of the imaged molecules is significantly less than the scanning speed, which is true for crystalline but not for liquid-like layers. In addition, the physisorbed layer next to the surface may be strongly bound and thus only suffer a minor perturbation due to the tip's presence. However, the following layers are much more weakly bound and thus are more easily affected. For dense multi-layers of n-alkanes on graphite<sup>17</sup>, for instance, the average molecular dynamics adsorption or surface energy of the second layer is only  $\sim 8\%$  of the average adsorption energy of the first layer. An apparatus better suited to study the normal structure of the interface is the surface force apparatus (SFA)<sup>31</sup>, but the composition of the solvation shells is only indirectly reflected in the measured force distance relations. Also, the SFA studies the interface of two surfaces in contact, whereas one might also be interested in the unperturbed liquid-solid interface (i.e. in the context of fluid flow problems). Here, simulations can provide useful complementary information about the structure and composition of complicated multi-component interfaces.

One example, which addresses the preferential adsorption, of one species of a binary mixture is an extension of the above simulation<sup>16</sup>. Now the system is larger and consists of 72 benzene and 400 heptane molecules (benzene mole fraction  $x_o^b=0.18$ ) and 216 benzene and 240 heptane molecules (benzene mole fraction  $x_o^b=0.474$ ), respectively. Figure 5 shows both the number of molecular centers of mass  $N$  and the local benzene mole fraction  $x^b$  as functions of distance from the graphite surfaces. Each panel includes the final 1.5ns of a 3.0ns run. In both panels the pronounced peaks at  $\sim 4\text{\AA}$  above the surface correspond to dense monolayers of heptane, whose occupancy is only slightly different for the two mole fractions. However, there is a strong qualitative difference for  $x^b$ . For  $x_o^b=0.18$  the range between  $\sim 8\text{\AA}$  and  $\sim 18\text{\AA}$  is enriched with benzene, i.e.  $x^b > x_o^b$ , whereas beyond  $\sim 18\text{\AA}$  there is a depletion of benzene, i.e.  $x^b < x_o^b$ , relative to the same system without the adsorbing surfaces. For  $x_o^b=0.474$ , on the other hand, no such inversion is observed. The point here is that the experimentally determined quantity  $\Delta x^\alpha = x_o^\alpha - x_{bulk}^\alpha$ , i.e. the change in bulk concentration of species  $\alpha$  on contact with

the solid, is often used to determine the preferential adsorption of  $\alpha$  (i.e.  $\Delta x^\alpha < 0$ ) for binary mixtures (cf. <sup>32,33</sup> for heptane/benzene). However, it is important to realize that the so determined preferential adsorption (e.g., via experimental methods like the measurement of the amount adsorbed or calorimetric studies) is really an average across the width of the interface, whereas, as the simulation reveals and as figure 5 (A) exemplifies, the other species may still preferentially occupy the layer closest to the surface.



**Figure 5:** Molecular center of mass distribution in terms of the number of molecules  $N$  (left axis) and benzene mole fraction  $x^b$  (right axis) as a function of distance from the graphite surfaces. Panels (A) and (B) are for two different compositions; i.e. 72 benzene and 400 heptane molecules (A) and 216 benzene and 240 heptane molecules (B). Thin solid lines: heptane center of mass distribution; thick solid lines: benzene center of mass distribution; short dashed lines: benzene mole fraction; horizontal long dashed lines: benzene mole fraction in the absence of the surfaces  $x_0^b$ . The error bars indicate the mean square deviations.

## 2.2 A simple analytical model for nematic, columnar, and crystalline phases in dense two-dimensional alkane layers

Even though the computer simulation is a powerful tool there are many phenomena beyond the present range of this method. The dense monolayers on which we focus here are not just crystalline but may exhibit other types of ordering depending on both temperature and molecular weight<sup>34</sup>, i.e. the alkane chain length, and, in addition for bi-disperse solutes, on the adsorbate composition (see also<sup>35</sup>). One example is shown in figure 6 taken from reference<sup>19</sup>, which displays a series of three STM images of mixed alkane monolayers containing  $C_{25}H_{52}$  and  $C_{50}H_{102}$ , adsorbed from concentrated but not saturated solutions in 1-phenyloctane at a total concentration of 7 mg/ml and a molar ratio between long and short molecules of around  $10^{-4}$ . Panels (a) and (c) exhibit crystalline phases, where the monolayer consists predominantly of  $C_{25}H_{52}$  and  $C_{50}H_{102}$ , respectively. At an intermediate mixing ratio, panel (b) shows a columnar phase in the sense that the molecules show crystalline ordering perpendicular to their molecular axes but appear fluid-like along the molecular axes, which makes it impossible to observe molecular ends on the STM-time scale, i.e. on the order of milliseconds. It should be noted that the considerable difference in molecular weight implies a strong tendency for preferential adsorption of the longer component, which means that one has to use the shorter component in large excess in the bulk solution. Thus, the experiment is subject to two main difficulties, i.e. a lack of control regarding the surface density (cf. below) as well as the fact that mixed monolayers are not stable as long as they are in contact with a solution containing longer chains (cf. also<sup>37</sup>). Fortunately, in the system chosen here the exchange between surface layer and bulk solution appears to be sufficiently slow compared to the development of two-dimensional order within the surface layer, so that the different types of ordering can be observed.

In three dimensions, liquid crystalline behavior of large shape-anisotropic molecules is often well approximated by hard particle excluded volume theories. Here I briefly want to discuss the application of one such approach to the above experimental system. The approach is based on an excluded volume model for lyotropic liquid crystalline behavior of mono-disperse orientationally ordered hard rigid spherocylinders in three dimensions<sup>38</sup>. Within this model the various possible translationally ordered phases are based on the tradeoff of translational entropy between translationally disordered liquid-like dimensions and translationally ordered crystal-like dimensions. The key idea is to approximate the dimensionless configurational free energy per particle in each phase as  $f_d^{conf} = \ln \rho - 1 + f_d^{fluid} + f_{D-d}^{cryst}$ , where  $\rho$  is the particle number density,  $D$  is the space dimension, and  $f_d^{fluid}$  is the non-ideality contribution from  $d$  fluid-like dimensions, whereas  $f_{D-d}^{cryst}$  is the non-ideality contribution from the remaining  $(D-d)$  crystal-like dimensions. Thus, in  $D=3$  dimensions,  $d=3$  for a nematic fluid,  $d=2$  for a smectic phase (i.e. two fluid dimensions and one crystalline dimension),  $d=1$  for a columnar phase (i.e. one fluid dimension and two crystalline dimensions), and  $d=0$  for a crystalline phase (i.e. three crystalline dimensions). Good approximations for the non-ideality contributions to  $f_d^{conf}$  can be obtained by using the scaled particle approach for  $f_d^{fluid}$ , whereas for  $f_{D-d}^{cryst}$  simple one particle cell models are quite adequate.

To describe the above experimental system, we consider an analogous bi-disperse two-dimensional model, which requires a number of crude but not too crude approximations. First we neglect the details of the interaction of the physisorbed monolayer with the rest of the interface and just confine the molecules to move in two dimensions. In a second step we replace the alkane chains by hard spherocylinders of corresponding length and width (cf. bottom part of figure 1). Finally, we consider three different types of ordering of the spherocylinders, i.e. crystalline, columnar, and nematic. The nematic phase is simply a two-dimensional fluid of oriented spherocylinders. In the model columnar phase the particles retain fluid-like behavior only in the direction of their long axis, whereas in the orthogonal direction they are confined between hard walls. The picture is that of a one-dimensional fluid of rods within a hard channel corresponding to a one-dimensional cell.

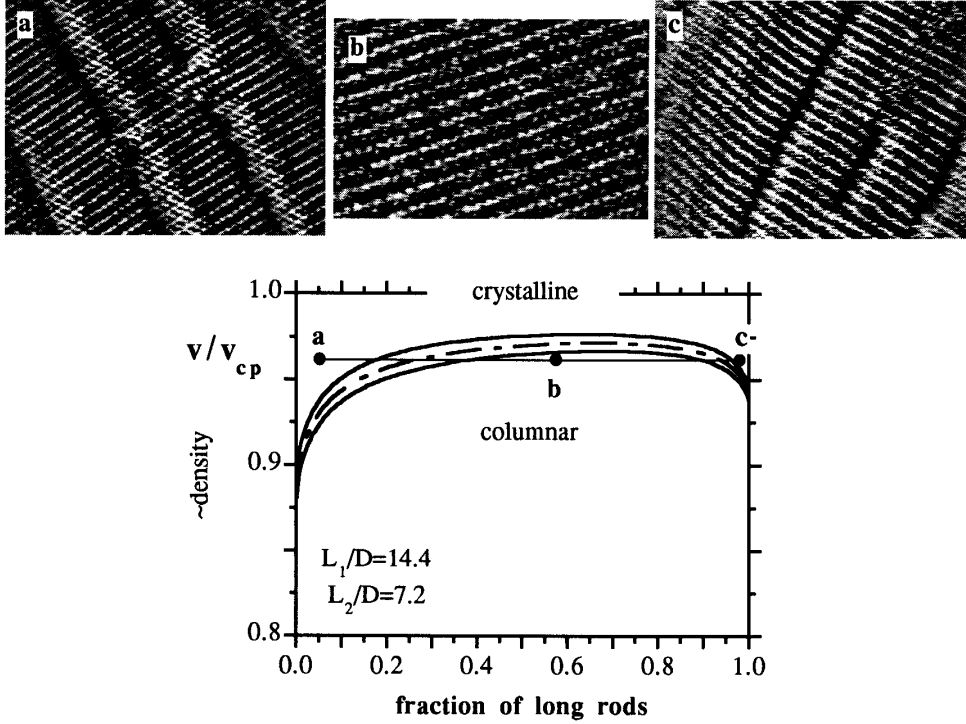


**Figure 6:** Top: STM images of a bi-disperse alkane monolayer of  $C_{25}H_{52}$  and  $C_{50}H_{102}$  adsorbed at the interface between the basal plane of graphite and an organic solution. Panels (a) and (c) show crystalline phases of predominantly short and long rods, respectively, with small crystallites of the other component incorporated. In the center of panel (a), there are three neighboring  $C_{50}H_{102}$  molecules across the width of two  $C_{25}H_{52}$  lamellae. In the lower right of panel (c), there are seven neighboring pairs of  $C_{25}H_{52}$  molecules within a  $C_{50}H_{102}$  lamella. Panel (b), on the other hand, shows a columnar phase. Using the graphite lattice, underlying the image, as an internal reference<sup>36</sup>, one finds that the columns of molecular rods are oriented parallel to a graphite lattice axis with a regular spacing between the columns, which is commensurate with the graphite lattice and equal to the intermolecular spacing in the crystalline alkane lamellae. The mobility along the columns is too high to allow the observation of the ends of the molecules. Notice that the 'graininess' in panel (b) is due to the graphite 'shining through'. Bottom: Partial theoretical phase diagram of the bi-disperse mixture in terms of the fraction of longer rods and the reduced volume fraction  $v/v_{cp}$ . Note that here  $v_{cp} = \sum_{i=1}^2 y_i v_{cp,i}$ , where  $v_{cp,i} = (\pi^2 / (8\sqrt{3}) + L_i / D) / (\pi / 4 + L_i / D)$ , is the volume fraction at close packing. In the phase diagram, solid lines indicate phase coexistence, and long-short dashes indicate the cross over between the columnar and the crystalline free energies.

In the crystalline phase, finally, each particle is confined within an impenetrable hard cell. Under these assumptions the configurational free energy of the binary mixture can approximately be written as

$$f_d^{conf} = \ln \rho - (1 - \delta_{0d}) + \sum_{i=1}^2 y_i \ln y_i + f_d^{fluid} + f_{2-d}^{crystal} \quad (5)$$

non-interacting point particles of type  $i=1,2$ , where the  $\delta$ -function accounts for the distinguishability of the particles in the crystalline phase. As where  $y_i$  denotes the fraction of particles of length  $L_i$ . The first three terms are the contribution of before in three dimensions,  $f_d^{fluid}$  is the excluded volume

contribution to the free energy of a  $d$ -dimensional fluid, and  $f_{D-d}^{cryst}$  is the free energy contribution accounting for the reduction of the available cell volume within a  $(2-d)$ -dimensional crystal due to the finite size of the particles. One can now compare the different free energies to determine the stable phase corresponding to the lowest free energy for a given set of the parameters, i.e. volume fraction  $v$ , particle fraction of type  $i$   $y_i$ , and aspect ratios  $L_i/D$  (Here  $D$  is the molecular diameter!). Phase diagrams can be calculated in the usual fashion equating the pressures  $p_d$  and the chemical potentials  $\mu_d = f_d + p_d/\rho$ .

The details of this calculation are described in reference <sup>19</sup>. Here I just present the result pertaining directly to the above experimental situation. The high density portion of the theoretical phase diagram (for aspect ratios  $L_i/D$  corresponding to the above molecular dimensions, i.e.  $L_1/D=14.4$  and  $L_2/D=7.2$ ) shown in figure 6 contains two phases, i.e. the columnar phase and the crystalline phase, as a function of reduced volume fraction and mixing ratio. Most noteworthy is the curvature of the crystalline-columnar coexistence region which allows the possibility of a crystalline-to-columnar-to-crystalline phase sequence as a function of the mixing ratio in a small range of high surface densities. Indeed, the sequence of STM images in figure 6 is consistent with a cut at  $v/v_{cp} \sim 0.95-0.97$  (corresponding to surface densities, which are in accord with what can be deduced from the STM images) through the theoretical phase diagram, i.e. one passes from a crystalline phase predominantly composed of short chains through a columnar phase back into a crystalline phase predominantly composed of longer chains.

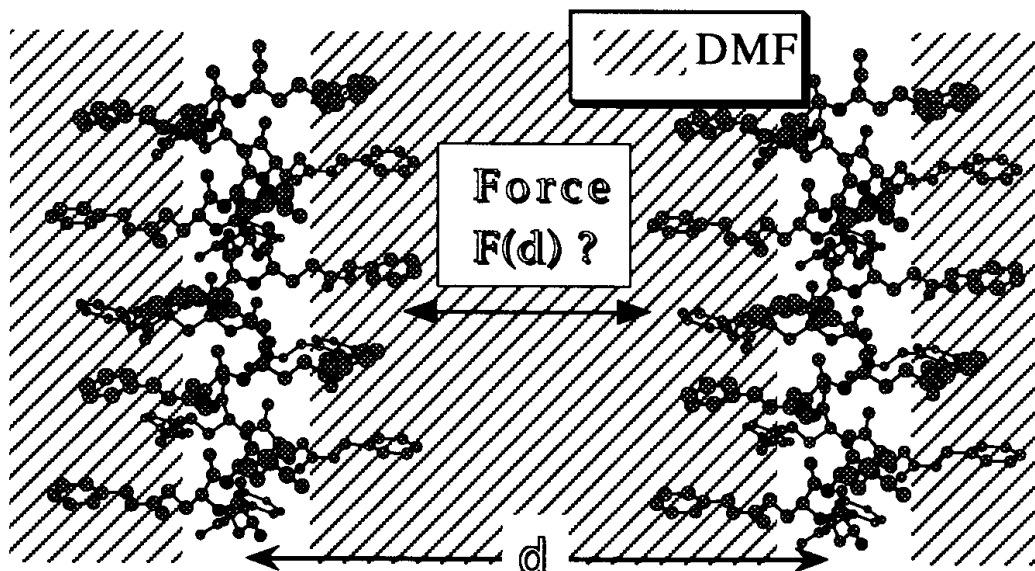
As pointed out above, the model used here is quite crude, e.g., it is athermal, it neglects fluctuations, and it certainly simplifies the molecules and their interactions drastically. Nevertheless, it provides a number of interesting insights, and some of the approximations can be improved. Also, the model correctly reproduces the observed high density surface phase behavior of mono-disperse  $n$ -alkanes as a function of molecular weight. However, a more detailed discussion would lead to far at this point and the interested reader is again referred to <sup>19</sup> and the references therein.

### 3. Molecular interaction in liquids: PBLG in DMF

In this section I want to return to the application of MD simulations and briefly address the interaction between surfaces in liquids. Clearly, there is much to be gained from understanding the forces between two interacting surfaces on the molecular level <sup>31</sup>. For instance, in the context of surface force microscopy it is the key to the detailed interpretation of the images. As we have already seen in the case of the liquid-solid interface, the presence of a surface induces a pronounced structure in the liquid, and thus the local density near the surface differs substantially from the bulk density and shows pronounced variations on the molecular scale. Such effects and their consequences, like the local variation of the dielectric properties of a material, have to be included in theoretical models aimed at the calculation of images obtained by tip microscopes. Again, simulations provide a magnifying glass through which tip-surface or surface-surface interactions can be observed on the molecular scale. Two nice examples are the molecular dynamics simulation of the interaction of a nickel tip with a bare gold surface <sup>39</sup> as well as with a gold surface <sup>23</sup> covered by a thin liquid alkane film and the simulation of a SFA containing thin films of linear and branched octane <sup>40</sup>. These simulation allow a close look at the relation between the structure of a confined liquid and the corresponding surface force at a given separation between a tip and a surface or between two plane surfaces.

In the following I want to discuss a third and somewhat different example of two interacting surfaces, which looks at the effective interaction between segments of two macromolecules in solution<sup>41</sup>. Figure 7 shows a schematic of the system, which consist of two parallel oriented segments of Poly( $\gamma$ -benzyl-L-glutamate) (PBLG), a helical polypeptide, which are dissolved in Dimethylformamide (DMF). PBLG is a fairly stiff polymer (with a persistence length of about 1000Å) due to the H-bonds stabilizing its backbone <sup>42</sup>. Due to this PBLG is a lyotropic liquid crystal, and it is itself or with modified side chains often used to prepare highly ordered films on solid substrates. Again, knowing the interaction forces is useful for the understanding of the formation of liquid

crystalline phases and the structures formed by the molecules on solid substrates. In addition, PBLG is a fairly 'thick' molecule with a diameter of  $\sim 16\text{-}20\text{\AA}$  depending on its surroundings (cf. below), so that, from the point of view of the simulation, the interaction between two segments is not too different from the interaction between two surfaces covered with PBG molecules (cf. the typical system sizes discussed above). As before, the potential function described by equation (1) can be used also in this case. However, the surface potential is now replaced by an additional 10-12 potential term, which, together with the Coulomb interactions, is used to describe the C=O...H-N hydrogen bonds between the  $n$ th and the  $(n+4)$ th peptide unit along the backbone.



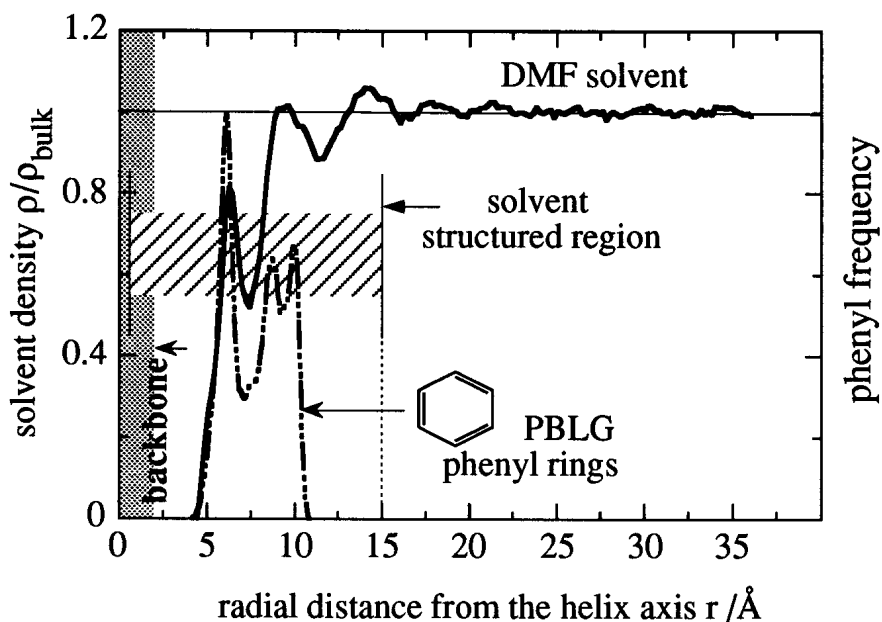
**Figure 7:** Schematic of two parallel oriented PBLG segments shown in ball-and-stick representation. The shading indicates the solvent, DMF. The length of each segment is  $27.04\text{\AA}$ , i.e. the repeat distance of the helix. In the simulation, periodic boundaries are applied to the system, so that each segment is covalently bound to its neighboring image segment. The size of the simulation box perpendicular to the helix axis is  $90\text{\AA} \times 60\text{\AA}$  (with a total particle number of  $\sim 6300$ ) in order to achieve bulk-like behavior of the solvent at large distances from the helix.

Figure 8, taken from reference <sup>42</sup>, is the PBLG's analog to the upper right panel in figure 4, i.e. it shows the DMF density profile as a function of the radial distance  $r$  from the helix center. Despite the side chains one again finds a pronounced solvation shell structure as before for the flat smooth surface, where the oscillations correspond to the size of the solvent molecules. Figure 8 also shows the center of mass distribution of the phenyl rings terminating the side chains, and it is interesting how the side chain distribution is split between the first two solvation shells to optimize mixing with the solvent.

Figure 9, taken from reference <sup>41</sup>, shows the force acting between the segments as a function of their separation  $d$ . For segment separations  $d$  greater than  $20\text{\AA}$  the force is zero within the scatter of the method. At about  $19\text{\AA}$  there is a threshold beyond which the force increases noticeably for decreasing  $d$  in addition to exhibiting oscillations until it finally diverges at  $\sim 8\text{\AA}$ . Notice that the force is repulsive for all  $d$  in contrast to the solid line in figure 9, which shows the LJ interaction of two corresponding solid cylinders. The overall repulsion might be due to the entropy loss, which the side chains suffer if their density increases due to the mutual penetration of the 'brushes'. But other reasons based on the entropy and enthalpy of the side chain-solvent interface must be considered also. This is discussed in somewhat greater detail in <sup>41</sup>. However, one can quite easily connect the structural changes in the interface between the segments and features in the force curve as a function of  $d$ . Figure 10 shows the solvent density profile along a narrow slab, whose right and left boundaries are the two back bones.

The three profiles are for separations  $d$ , which bracket the local force maximum marked by (x) in figure 9. The solid line in figure 10 gives the profile for  $d$  roughly at the local minimum to the right of (x). This profile shows two well formed solvent layers between the segments. The dashed-dotted line gives the corresponding profile for a  $d$ , which roughly coincides with the local minimum to the left of (x). Now there is only one layer. Again, we find what one already knows from smooth flat surfaces (e.g., <sup>31,40</sup>), i.e. the perturbation of the solvation shells gives rise to an increase in the interaction force.

I want to conclude this section with a last look at the data points shown in figure 9. These data points are deduced from experimental solvent activities  $a_{DMF}$  at high concentrations <sup>43</sup>, relating  $a_{DMF}$  to the osmotic pressure  $\pi$  via  $a_{DMF} \approx \exp(-\pi V_{DMF} / RT)$ , where  $V_{DMF}$  is the molar volume of DMF. Assuming hexagonal packing of the PBLG molecules at high concentrations one can very roughly express it in terms of the force  $F(d)$  between two neighboring segments by  $\pi \approx \sqrt{3} F(d) / (Ld)$ , where  $L$  is the segment length and  $(Ld) / \sqrt{3}$  the area of one face of the hexagonal cell. Similarly, it is possible to estimate the experimental  $d$  via  $d = d_{crystalline} / \sqrt{v}$ , where  $d_{crystalline} \approx 15.4 \text{ \AA}$  is the experimental separation between helices in the crystalline state <sup>42</sup> and  $v$  is the experimental DMF volume fraction. The point is that the data show an obvious kink at the position of the force threshold in the simulation at  $\sim 19 \text{ \AA}$ . Below  $d \sim 19 \text{ \AA}$  the estimated force rises quickly and is virtually independent of the molecular weight - consistent with a dense hexagonal packing. Above  $d \sim 19 \text{ \AA}$  the hexagonal packing is lost. Thus the force threshold defines an effective hard core radius of the PBLG molecule in solution. Notice that the much faster increase of the experimental force below  $\sim 19 \text{ \AA}$  is due to the larger number of neighboring PBLG molecules in comparison to the simulation.



**Figure 8:** Solvent density  $\rho$  divided by the bulk solvent density as a function of the radial distance  $r$  from the helix axis for a single isolated segment (solid line), and the corresponding distribution of the center of mass of the phenyl rings (broken line). The simulation was carried out in the NVT ensemble at room temperature <sup>42</sup>.

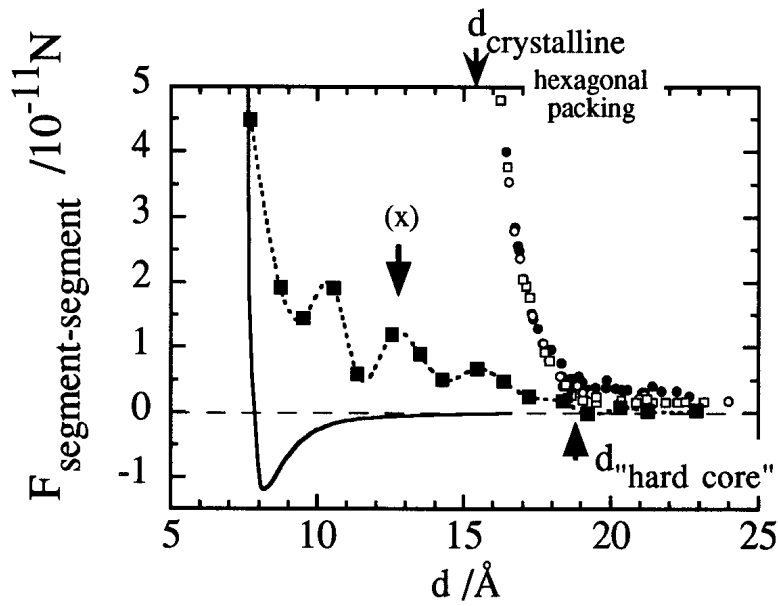


**Figure 9:** The force between the segments vs. their separation  $d$ . The solid squares connected by the dotted line are the simulation results (each square corresponds to a 200ps simulation at room temperature). The thin solid line gives the force between two parallel solid cylinders, whose atomic composition corresponds to the composition of the helix (analogous to the above 9-3 surface potential), interacting via LJ pair potentials. The symbols are estimates based on experimental activity data obtained for different molecular length PBLG (solid circles:  $\sim 1000\text{\AA}$ ; hollow circles:  $\sim 420\text{\AA}$ ; hollow squares:  $\sim 140\text{\AA}$ ).

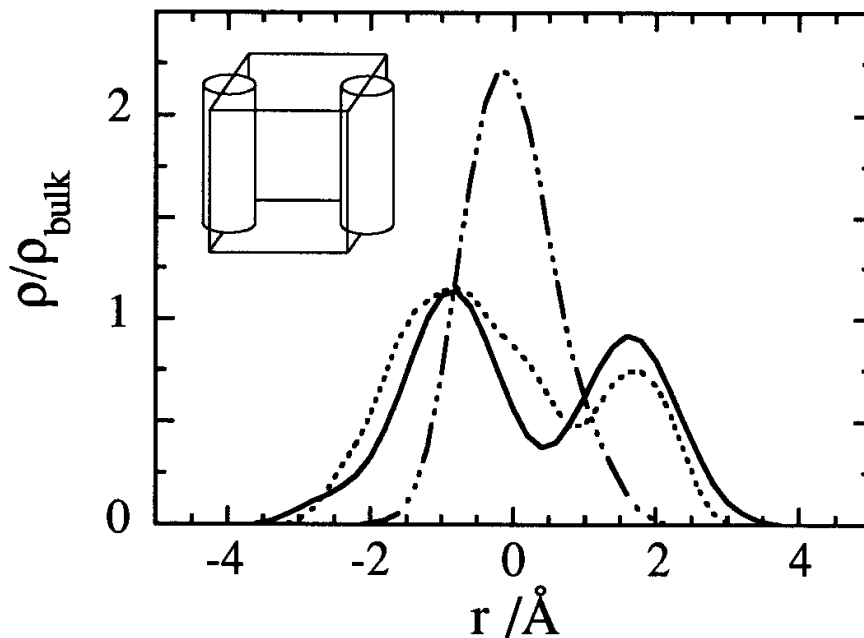


**Figure 10:** Solvent density  $\rho$  divided by the bulk solvent density in a thin ( $6\text{\AA}$  wide) slab between the two segments (cf. the sketch) for different segment separations, where  $r=0$  corresponds to the middle of the perpendicular connection of the two segment axes<sup>41</sup>. Solid line:  $d=13.6\text{\AA}$ ; dotted line:  $d=12.6\text{\AA}$ ; dashed-dotted line:  $d=11.4\text{\AA}$ . Notice that these segment separations  $d$  bracket the local force maximum indicated by (x) in the previous figure.

## Acknowledgements

I owe thanks to J. Helfrich for supplying figures 8-10 and to Prof. J.P. Rabe for numerous discussions on various aspects of this work.

## References

- (1) Butt, H. J.; Guckenberger, R.; Rabe, J. P. *Ultramicroscopy* **1992**, *46*, 375.
- (2) Swalen, J. D.; Allara, D. L.; Andrade, J. D.; Chandros, E. A.; Garoff, S.; Isrealachvili, J.; McCarthy, T. J.; Murray, R.; Pease, R. F.; Rabolt, J. F.; Wynne, K. J.; Yu, H. *Langmuir* **1987**, *3*, 932.
- (3) *Adsorption from Solution at the Solid/Liquid Interface*; Parfitt, G. D.; Rochester, C. H., Ed.; Academic Press: London, 1983.
- (4) Abraham, F. F.; Rudge, W. E.; Auerbach, D. J.; Kock, S. W. *Phys. Rev. Lett.* **1984**, *52*, 445.
- (5) Rowley, L. A.; Nicholson, D.; Parsonage, N. G. *Mol. Phys.* **1976**, *31*, 365.
- (6) Steele, W. A.; Vemov, A. V.; Tildesley, D. J. *Carbon* **1987**, *25*, 7.
- (7) Joshi, Y. P.; Tildesley, D. J.; Ayres, J. S.; Thomas, R. K. *Mol. Phys.* **1988**, *65*, 991.
- (8) Ruiz-Suarez, C. J.; Klein, M. L.; Moller, M. A.; Rowtree, P. A.; Scoles, G.; Xu, J. *Phys. Rev. Lett.* **1988**, *61*, 710.
- (9) Severin, E. S.; Tildesley, D. J. *Mol. Phys.* **1980**, *41*, 1401.
- (10) Nosè, S.; Klein, M. L. *Phys. Rev. Lett.* **1984**, *53*, 818.
- (11) Moller, M. A.; Klein, M. L. *J. Chem. Phys.* **1989**, *90*, 1960.
- (12) Hentschke, R.; Schürmann, B. L. *Surf. Science* **1992**, *262*, 180.
- (13) Leggetter, S.; Tildesley, D. J. *Mol. Phys.* **1989**, *68*, 519.
- (14) Hansen, F. Y.; Newton, J. C.; Taub, H. *J. Chem. Phys.* **1993**, *98*, 4128.
- (15) Xia, T. K.; Landman, U. *Science* **1993**, *261*, 1310.
- (16) Kotelyanskii, M. J.; Hentschke, R. *Phys. Rev. E* **1994**, *49*, 910.
- (17) Hentschke, R.; Schürmann, B. L.; Rabe, J. P. *J. Chem. Phys.* **1992**, *96*, 6213.
- (18) J.P. Rabe, private communication
- (19) Hentschke, R.; Askadskaya, L.; Rabe, J. P. *J. Chem. Phys.* **1992**, *97*, 6901.
- (20) Allen, M. P.; Tildesley, D. J. *Computer Simulations of Liquids*; Clarendon Press: Oxford, 1990.

- (21) *Computer Simulation in Material Science*; Meyer, M.; Pontikis, V., Ed.; Kluwer Academic Publishers: Dordrecht, 1991; Vol. 205.
- (22) Haile, J. M. *Molecular Dynamics Simulation*; John Wiley&Sons, Inc.: New York, 1992.
- (23) Landmann, U.; Luedtke, W. D.; Quyang, J.; Xia, T. K. *Jpn. J. Appl. Phys.* **1993**, *32*, 1444.
- (24) Weiner, S. J.; Kollman, P. A.; Case, D. A.; Singh, U. C.; Ghio, C.; Alagona, G.; Profeta, S.; Weiner, P. *J. Am. Chem. Soc.* **1984**, *106*, 765.
- (25) Weiner, S.; Kollman, P.; Nguyen, D. T.; Case, D. A. *J. Comp. Chem.* **1986**, *7*, 230.
- (26) Steele, W. A. *Surf. Science* **1973**, *36*, 317.
- (27) Cincotti, S.; Burda, J.; Hentschke, R.; Rabe, J. P. *submitted*
- (28) Battezzati, L.; Pisani, C.; Ricca, F. *J. Chem. Soc. Faraday Trans. II* **1629**, *71*, 1629.
- (29) Hentschke, R.; Winkler, R. *J. Chem. Phys.* **1993**, *99*, 5528.
- (30) Winkler, R.; Hentschke, R. *J. Chem. Phys.* **1993**, *99*, 5405.
- (31) Israelachvili, J. *Intermolecular and Surface Forces*; 2nd Edition ed.; Academic Press: New York, 1992.
- (32) Ash, S. G.; Brown, R.; Everett, D. H. *J. Chem. Thermodyn.* **1973**, *5*, 239.
- (33) Ash, S. G.; Brown, R.; Everett, D. H. *J. Chem. Soc. Faraday Trans.* **1975**, *171*, 123.
- (34) Askadskaya, L.; Rabe, J. P. *Phys. Rev. Lett.* **1992**, *69*, 1395.
- (35) Buchholz, S.; Rabe, J. P. *Angew. Chem. Int. Ed. Engl.* **1992**, *31*, 189.
- (36) Rabe, J. P.; Buchholz, S. *Science* **1991**, *253*, 424.
- (37) Gennes, P. G. d. *Adv. Colloid and Interface Sci.* **1987**, *27*, 189.
- (38) Taylor, M. P.; Hentschke, R.; Herzfeld, J. *Phys. Rev. Lett.* **1989**, *62*, 800.
- (39) Landmann, U.; Luedtke, W. D.; Burnham, N. A.; Colton, R. J. *Science* **1990**, *248*, 454.
- (40) Wang, Y.; Hill, K.; Harris, J. G. *Langmuir* **1993**, *9*, 1983.
- (41) Helfrich, J.; Hentschke, R. *submitted*
- (42) Helfrich, J.; Hentschke, R.; Apel, U. M. *Macromolecules* **1994**, *27*, 472.
- (43) Kubo, K. *Mol. Cryst. Liq. Cryst.* **1981**, *74*, 7 1.